Journal of Materials Chemistry A

ROYAL SOCIETY OF CHEMISTRY

PAPER

View Article Online
View Journal | View Issue

Cite this: *J. Mater. Chem. A*, 2020, **8**, 13150

Activating the lattice oxygen in $(Bi_{0.5}Co_{0.5})_2O_3$ by vacancy modulation for efficient electrochemical water oxidation†

Huan Liu,[a] Xiaoning Li,[b] Cailing Peng,[a] Liuyang Zhu,[a] Yuanxi Zhang,[a] Huiru Cheng,[c] Jiameng Cui,[a] Qingmei Wu,[a] Yingying Zhang,[a] Zezhi Chen,[a] Wei Zou,[a] Wen Gu,[a] Haoliang Huang,[bd] Jianlin Wang,[bd] Bangjiao Ye,[c] Zhengping Fu*[abd] and Yalin Lu*[abd]

Received 26th March 2020
Accepted 11th June 2020

DOI: 10.1039/d0ta03411h

rsc.li/materials-a

The catalytic activity for the oxygen evolution reaction (OER) in electrocatalytic water splitting strongly depends on the adsorption energy of intermediates. For the generally proposed adsorbate evolution route, the universal scaling relation between the adsorption energies of *OOH and *OH leads to an OER efficiency limitation based on the "volcano curve". A possible solution to bypass the scaling relation is to avoid the formation of the *OOH intermediate in the OER with the participation of lattice oxygen from catalysts. In this work, the lattice oxygen in $(Bi_{0.5}Co_{0.5})_2O_3$ is activated through adjusting the Fermi energy level and the strong overlap between Co 3d and O 2p, by means of increasing the oxygen vacancy concentration. Compared to oxygen-vacancy-poor $(Bi_{0.5}Co_{0.5})_2O_3$, the oxygen-vacancy-rich $(Bi_{0.5}Co_{0.5})_2O_3$ exhibits a significantly lower Tafel slope (43 mV dec^{-1}), 15 times higher mass activity, 18 times higher turnover frequency, and excellent long-term stability in alkaline media, superior to those of the benchmark OER electrocatalyst IrO_2. This work provides a feasible strategy to activate lattice oxygen with fast OER kinetics and puts forward the development of efficient and stable catalysts towards water oxidation.

Introduction

The kinetically sluggish oxygen evolution reaction (OER) is the rate-determining step in electrocatalytic water splitting.[1–3] It is vital but still a big challenge to develop efficient electrocatalysts with small overpotentials and good stability through understanding and thus rational control of the OER route. Generally, the OER involves four intermediate oxygen species, starting from adsorbed *OH (* marks an active site) to *O, and two possible routes are proposed for the subsequent O–O formation step. In the conventional adsorbate evolution mechanism (AEM), which is a single active site mechanism, complex four-step proton-coupled electron transfer processes are involved,[4] and the O–O bond is formed through nucleophilic attack of *O by water or OH^-, which results in the formation of *OOH. The adsorption energies of different species (*OH, *O, and *OOH) linearly scale with each other, and the scaling relation between *OOH and *OH is universal for materials and might be the origin of OER efficiency limitations in a conventional "volcano curve".[5,6] From the thermodynamic perspective, the optimal adsorption energy difference between *OOH and *OH is 2.46 eV, but the value is generally near 3.2 eV, leading to a high energy barrier.[5,7,8] Thus, high OER performance is possible only if the scaling relation between *OOH and *OH is broken *via* bypassing the generation of the *OOH intermediate. Two effective routes have been proposed up to now. One involves O–O formation *via* direct coupling of two *O species on two adjacent sites. The other involves O–O formation *via* coupling between lattice oxygen and *O, and this is named the lattice oxygen oxidation mechanism (LOM).[5,9] Basically, the coupling of *O on two adjacent active sites seldom happens due to its high requirements on the geometric and electronic structures.[10] In contrast, LOM with a lower reaction barrier is comparatively feasible to achieve by rational design, as has been demonstrated both theoretically and experimentally.[9,11–16] The OER *via* LOM is a non-concerted proton–electron transfer process, which is characterized by a strong pH-dependent performance. For example, Yang Shao-Horn's group triggered lattice oxygen

[a]*Department of Materials Science and Engineering, CAS Key Laboratory of Materials for Energy Degradation, University of Science and Technology of China, Hefei 230026, P. R. China. E-mail: fuzp@ustc.edu.cn; yllu@ustc.edu.cn*

[b]*Synergetic Innovation Center of Quantum Information and Quantum Physics, Hefei National Laboratory for Physical Sciences at Microscale, University of Science and Technology of China, Hefei 230026, P. R. China*

[c]*State Key Laboratory of Particle Detection and Electronics, University of Science and Technology of China, Hefei 230026, P. R. China*

[d]*Anhui Laboratory of Advanced Photon Science and Technology, University of Science and Technology of China, Hefei 230026, P. R. China*

† Electronic supplementary information (ESI) available. See DOI: 10.1039/d0ta03411h

activation in perovskite $LaCoO_{3-\delta}$ *via* adjusting the covalency of metal–oxygen bonds by Sr doping on La sites, with solid evidence from *in situ* ^{18}O isotope labeling mass spectrometry.[15] Wang's group incorporated Zn^{2+} into CoOOH to generate the Zn–O bond together with non-bonding oxygen among the original Co–O bonds, resulting in the direct coupling of two neighboring O–O evidenced by chemical recognition.[9] Li' group adjusted the Co intermediate spin state to high valence 4+, making two $-O^-$ form a surface peroxide ion in $CaCoO_3$ *via* high temperature and ultrahigh pressure synthesis.[16] These electrocatalysts reported with LOM are the most promising candidates compared to other OER active materials.

To activate LOM, generating sufficient surface oxygen vacancy defects may be a good choice, as the electronic structure is strongly related with the surface of catalysts.[9,14–16] The Fermi energy level and the orbital overlap between cations and oxygen anions can be adjusted by controlling the surface oxygen vacancies,[14,17,18] as the absence of oxygen weakens the coulombic force of adjacent cations and anions. Transition metal (Fe, Co or Ni) oxides have been regarded as promising OER catalysts and the metal cations are generally considered as active species.[19–22] They have great potential to be activated with LOM, with a tunable crystal and electronic structure by cation substitutions or defect engineering. However, LOM-active perovskites usually show poor stability and tend to become amorphous during long operation in alkaline solutions when the O p-band is close to the Fermi level.[10] For example, the $SrCoO_{3-\delta}$ based perovskites $Ba_{0.5}Sr_{0.5}Co_{0.8}Fe_{0.2}O_{3-\delta}$ (BSCF) and $SrCo_{0.8}Fe_{0.2}O_{3-\delta}$ (SCF) readily undergo the formation of the amorphous phase in the surface, and the structure switches from corner-sharing to edge-sharing CoO_6 octahedra.[23–25] When the O p-band is too close to the Fermi level, lattice oxygen participation *via* reversible formation of surface oxygen vacancies is essential due to ineffective electron donation by the B-site cation.[11] Thus, it is desirable to develop a catalyst system with fast LOM and high stability in the long term OER operation.

$(Bi_{0.5}Co_{0.5})_2O_3$, a tetrahedral structure derived by substituting half of the Bi in Bi_2O_3 with Co and composed of a CoO_4 and BiO_4 tetrahedron (BCO, Fig. S1†), may potentially be a highly efficient and stable OER electrocatalyst with LOM based on the following analysis. The bond length of Co–O is short enough to ensure a large overlap between Co 3d and O 2p orbitals, which could make LOM possible by slight manipulation, just as the cases of perovskite OER electrocatalysts with LOM. In addition, there are still quite a few research studies indicating that tetrahedrally coordinated active sites in spinel oxides with π-type interaction are OER-active. As reported, both the tetrahedral Co ions and the octahedral oxygen ions on the surface are active in $Ba_4Sr_4(Co_{0.8}Fe_{0.2})_4O_{15}$ with ultrahigh OER activity.[26] Furthermore, different from the instability induced by the excessively strong overlap between metal 3d and O 2p orbitals within octahedra in perovskite oxides,[25,27] BCO may exhibit a better OER stability because the interaction between active sites and oxygen species is π-type interaction (side-to-side overlap) in tetrahedra, which is not as strong as the σ-type interaction (head-to-head overlap) in perovskites.[10] At the same time, bismuth is comparatively easier to volatilize at high temperature during the materials synthesis, which could help to stably retain more oxygen defects that are desired for LOM activation.[28] In fact, Bi-based oxides have been extensively explored in electrocatalysis. For instance, Bi_2O_3 nanosheets grown on a conductive multiple channel carbon matrix exhibit high energy efficiency and long-term stability for the CO_2 reduction reaction.[29] The e_g electron is tuned by *in situ* growth of $BiCoO_3$ on $Bi_5CoTi_3O_{15}$ to promote OER activity.[2,30]

With these considerations in mind, a surface-oxygen-vacancy strategy is adopted in this work to enhance the hybridization between Co 3d and O 2p orbitals to activate the lattice oxygen in BCO. The oxygen vacancy concentration is modulated by the heat treatment of the precursor under different atmospheres. The surface oxygen vacancies not only increase the ion mobility and conductivity but also activate the LOM-type OER process, which is evidenced by the pH-dependent activity and chemical probe analysis of peroxo-like species (O_2^{2-}). XPS and XAS investigations reveal that highly oxidative oxygen species (O_2^{2-}/O^-) and surface oxygen anions are the dominant redox partners to molecular oxygen due to strong hybridization between oxygen 2p and transition metal 3d electron states. The as-prepared oxygen-vacancy-rich catalysts show much better OER efficiency and long-term stability than the state-of-the-art IrO_2. This work provides a new insight to activate lattice oxygen *via* surface defects and crystal structure modulation.

Results and discussion

Characterization of BCO catalysts

The synthesis process of BCO is schematically illustrated in Fig. 1a. The precursor was prepared by coprecipitating Bi^{3+} and Co^{2+} ions, followed by heat treatment under air and oxygen atmospheres, respectively. The sample treated in air is denoted as V_o-rich BCO, and the sample treated under the oxygen atmosphere is denoted as V_o-poor BCO. Inductively Coupled Plasma-Atomic Emission Spectroscopy (ICP-AES) analysis was conducted to quantify the ratio of Bi to Co in BCO samples, in which the ratios are close to 1, as displayed in Table S1†.† The X-ray diffraction (XRD) patterns of the as-prepared samples are shown in Fig. 1b and c. We performed XRD refinement for the powders by the Rietveld method,[31] and the refined crystal structure parameters are listed in Table S2†.† The two samples can be indexed to the Bi_2O_3 structure, the R_{wp} value of V_o-rich BCO is 7.24%, and the R_{wp} value of V_o-poor BCO is 6.42%, which reflects the close agreement with the tetragonal structure of Bi_2O_3 (space group $P\bar{4}21c$). Rietveld refinement shows that the lattice parameters of the as-prepared V_o-rich BCO are $a = 7.731$ Å, $b = 7.731$ Å, and $c = 5.627$ Å, while those of V_o-poor BCO are $a = 7.737$ Å, $b = 7.737$ Å, and $c = 5.631$ Å. The lattice parameters indicate that V_o-rich BCO has a larger volume than that of V_o-poor BCO; therefore the distortion of V_o-rich BCO is greater than that of V_o-poor BCO, indicating that more oxygen defects are formed in V_o-rich BCO. Both scanning electron microscope (SEM) and transmission electron microscope (TEM) images indicate that BCO samples show a sheet-like morphology (Fig. S2† and 1d). The spacings of lattice fringes in the high-resolution transmission electron microscope (HRTEM) image of V_o-rich BCO are 2.74 Å and 2.81 Å, corresponding to the

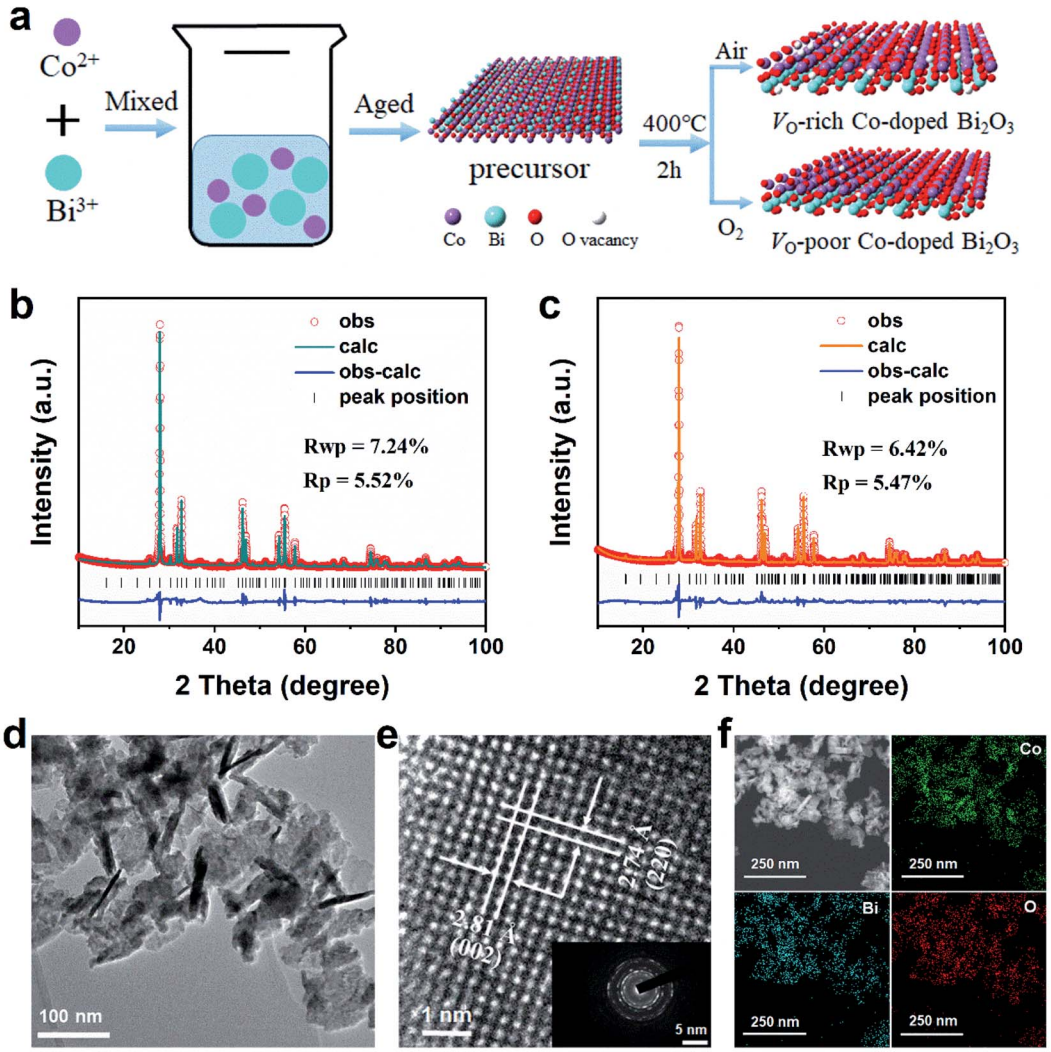

Fig. 1 (a) Schematic illustration of the preparation of BCO. XRD patterns of the as-prepared samples: (b) V_o-rich BCO; (c) V_o-poor BCO. (d) TEM image of V_o-rich BCO. (e) The high-resolution TEM image. The inset in (e) shows the corresponding SAED pattern. (f) EDS elemental mapping images of V_o-rich BCO.

interplanar spacing of the (220) and (002) planes of BCO (Fig. 1e). And the corresponding selected area electron diffraction (SAED) patterns of V_o-rich BCO show a polycrystalline feature. In addition, the energy dispersive spectroscopic (EDS) mapping results demonstrate that the spatial distribution of Bi, Co, and O is consistent (Fig. 1f). All structure and morphology results indicate that the nanostructured BCO has been successfully prepared.

Defect and electronic characterization

Considering that the electronic properties are influenced by defects,[14,18] X-ray photoelectron spectroscopy (XPS) analysis was conducted to investigate the surface component, electronic structure, and defect structure. As shown in Fig. 2a, two peaks with binding energies (BEs) of ~779.96 eV and ~795.00 eV are identified to be from $2p_{3/2}$ and $2p_{1/2}$ of Co^{3+}. The peak position of V_o-rich BCO shifts slightly to lower energy (about 0.31 eV), which confirms that the V_o-rich BCO sample has higher surface oxygen vacancy concentration according to previous reports that surface oxygen vacancies can decrease the oxidation state of Co.[19,20] As indicated in Fig. 2b, the O1s spectra can be deconvoluted into four characteristic peaks. The peak with the lowest BE (~529.7 eV) is attributed to the lattice oxygen species (O_L^{2-}), while the one with a BE of 531.1 eV can be ascribed to the highly oxidative oxygen species (O_2^{2-}/O^-).[1,32,33] The peak at around 532.3 eV is assigned to hydroxyl groups or the surface adsorbed oxygen (–OH/O_2), and the peak with the highest BE is ascribed to molecular water or carbonate ions adsorbed on the surface (CO_3^{2-}/H_2O). The relative contents of these four surface oxygen species are calculated from the corresponding peak areas and are summarized in Table S3.† The relative contents of O_2^{2-}/O^- in V_o-rich BCO are prominently higher than those in V_o-poor BCO, which may be a result of more oxygen vacancies in the surface layer of V_o-rich BCO. The results are in line with the trend of Co 2p results. Oxygen vacancies can weaken the coulombic force between lattice oxygen (O^{2-}) and metal ions,

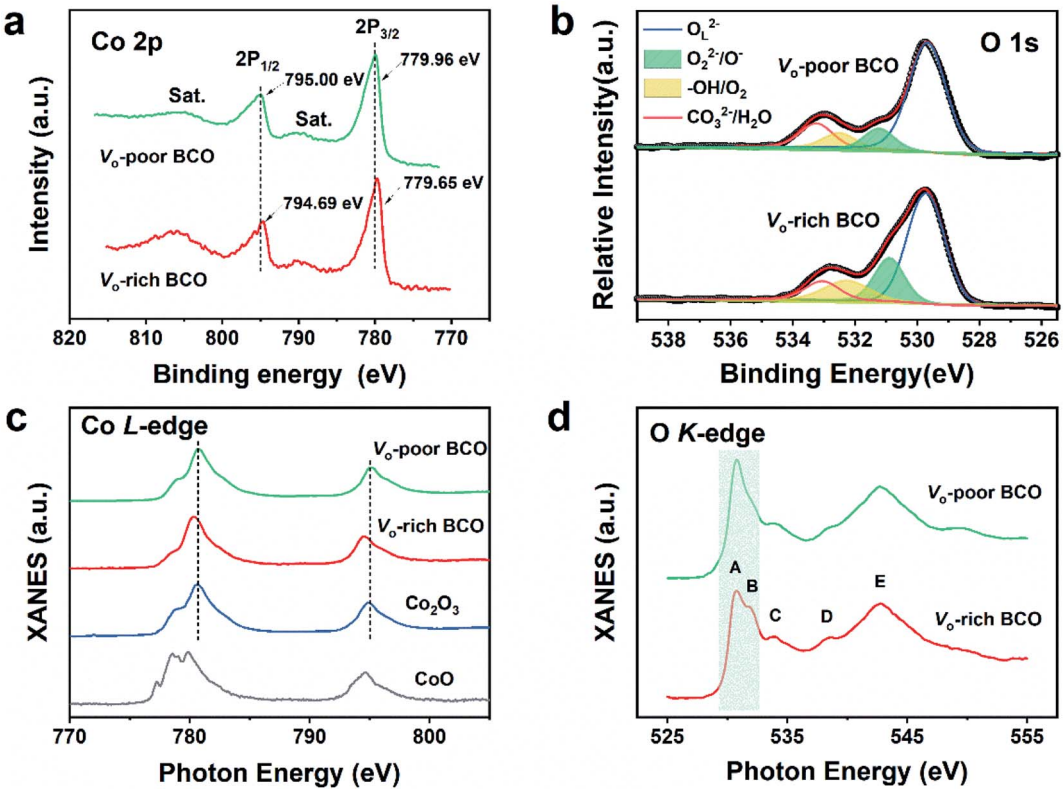

Fig. 2 (a) Co 2p XPS spectra. (b) O 1s XPS spectra. (c) Normalized Co L-edge XAS spectra. (d) Normalized O K-edge XAS spectra.

and thus facilitate the formation of active oxygen (O^-) or peroxo-like species (O_2^{2-}).[1,32] The Bi 4f spectra in Fig. S3† indicate that there is no distinct difference in the Bi oxidation state between V_o-rich BCO and V_o-poor BCO, and thus the impact of Bi on the subsequent OER activity can be excluded.

Soft X-ray absorption near-edge structure (XANES) measurement, which is more sensitive to the local chemical and structural environment and oxidation state, was conducted to detect the L-edge excitation of elemental Co and K-edge excitation of elemental O. As shown in Fig. 2c, there are two peaks located at around 780.7 eV (L_3) and 795.1 eV (L_2) due to the transition of core electrons from $2p_{3/2}$ and $2p_{1/2}$ hybrid orbitals to the O 2p orbital level, respectively. Compared with the standard reference CoO (Co^{2+}) and Co_2O_3 (Co^{3+}) $L_{2,3}$-edge, the oxidation states of Co in BCO can be roughly regarded as trivalent. It is noted that V_o-rich BCO exhibits a slight shift of the L edge by 0.4 eV compared to Co_2O_3 and V_o-poor BCO. This edge-shift value indicates that surface Co^{3+} ions in BCO are partially reduced to $Co^{3-\delta}$ by air sintering. Based on the electrical neutrality principle, the concentration of oxygen vacancies will be higher in V_o-rich BCO with $Co^{3-\delta}$, in line with the XPS studies of Co 2p and O 1s. This conclusion can be further justified by variation of O K-edge XAS spectra in Fig. 2d, in which features 'A' and 'B' are ascribed to the unoccupied states of e_g and t_{2g} states of Co 3d, respectively, which are generated by the hybridization of Co 3d and O 2p in the tetrahedral crystal field. Peaks 'D' and 'E' can be assigned to the electronic states with Bi 4d–O 2p character and Co 4sp–O 2p states, respectively. It should be noted that the amount of oxygen vacancy does not affect the shape or position of the features 'A', 'C', 'D' and 'E' observed in the O K-edge spectrum. However, the intensity of peak 'B' corresponding to unoccupied t_{2g} states is higher in V_o-rich BCO spectra than that in V_o-poor BCO. It is well known that the concentration of oxygen vacancies can influence the carrier concentration due to the electroneutrality, while the carrier concentration can modulate feature B in the O K-edge XAS. Thus the increased intensity of peak B in V_o-rich BCO is consistent with the depopulation of electronic states near the Fermi level. This higher peak in V_o-rich BCO indicates higher surface oxygen vacancy and a lower Fermi level,[14,34] which is indicative of strong hybridization between oxygen 2p and transition metal 3d electron states. The clear variation of t_{2g} peak intensity indirectly suggests that the oxygen is redox-active during the oxygen incorporation and evolution. Spin-polarized Density Functional Theory (DFT) computation was also carried out for BCO with and without oxygen vacancies (Fig. S4†). The projected densities of states (PDOSs) of Co 3d and O 2p are shown in Fig. S5.† The overlap of these two bands indicates orbital hybridization and Co–O bond formation. From Fig. S6a,† the overlap of these two bands in V_o-BCO is larger than that of BCO, which indicates the stronger hybridization between oxygen 2p and transition metal 3d electron states in V_o-BCO. Furthermore, the PDOS analysis demonstrates that the unoccupied states of V_o-BCO near the Fermi level are higher than those of BCO, and this is consistent with the O K-edge analysis in which peak 'B' rises in V_o-rich BCO.

To further confirm the oxygen vacancy, the compositions of the as-prepared catalysts were analyzed using an electron probe micro-analyzer (EPMA). The ratio of Bi/Co is close to 1 : 1 as shown in Table S4;† specifically, the ratio of O/(Bi + Co) is 1.38 and 1.42 in V_o-rich BCO and V_o-poor BCO, respectively. The deviation of oxygen stoichiometry δ is about 0.24 and 0.16 in V_o-rich BCO and V_o-poor BCO, respectively, which indicates that air sintering generates more oxygen vacancies in V_o-rich BCO. The Brunauer–Emmett–Teller (BET) surface area of V_o-rich BCO catalysts is larger than the value of V_o-poor BCO catalysts, which may be due to the more accessible vacancy sites. The details of the pore structure are shown in Fig. S6.† Positron annihilation spectroscopy (PAS) was applied to provide valuable information about the electronic and physical structure of vacancy defects.[35–38] In Fig. S7,† the positron lifetime spectra of both V_o-rich BCO and V_o-poor BCO yield three-lifetime components, where the middle component (τ_2) is usually ascribed to larger size defects such as oxygen vacancy clusters on the surface, while the shortest component (τ_1) comes from the small vacancies like mono-vacancies or shallow positron traps like oxygen vacancies in the bulk and the longest components (τ_3) may have resulted from the large void or interface in the materials (Table S5†). As expected, the intensity of the component (I_2) in V_o-rich BCO is higher than that in V_o-poor BCO, which reveals that more oxygen vacancies are generated on the surface in V_o-rich BCO. All the results above consistently verify the formation of more surface oxygen vacancies in V_o-rich BCO.

Catalyst activity and stability of oxygen-vacancy-rich BCO

To explore the influence of oxygen vacancies on the OER catalytic behavior, the OER activity of the as-prepared catalysts, benchmark IrO_2 (Aladdin Industrial Corporation) and carbon black catalysts was evaluated in 1.0 M KOH electrolyte by cyclic voltammetry (CV) and linear sweep voltammetry (LSV) at a scan rate of 5 mV s^{-1}, respectively. Fig. S8† shows the representative CV curves of BCO samples recorded within a potential window of 1.0–1.7 V (*vs.* RHE) and the positive-going OER curve without *iR*-correction. As shown in Fig. 3a, V_o-rich BCO exhibits good catalytic activity with a low overpotential of 367 mV, which is 3 mV and 85 mV lower than those of IrO_2 (overpotential of 370

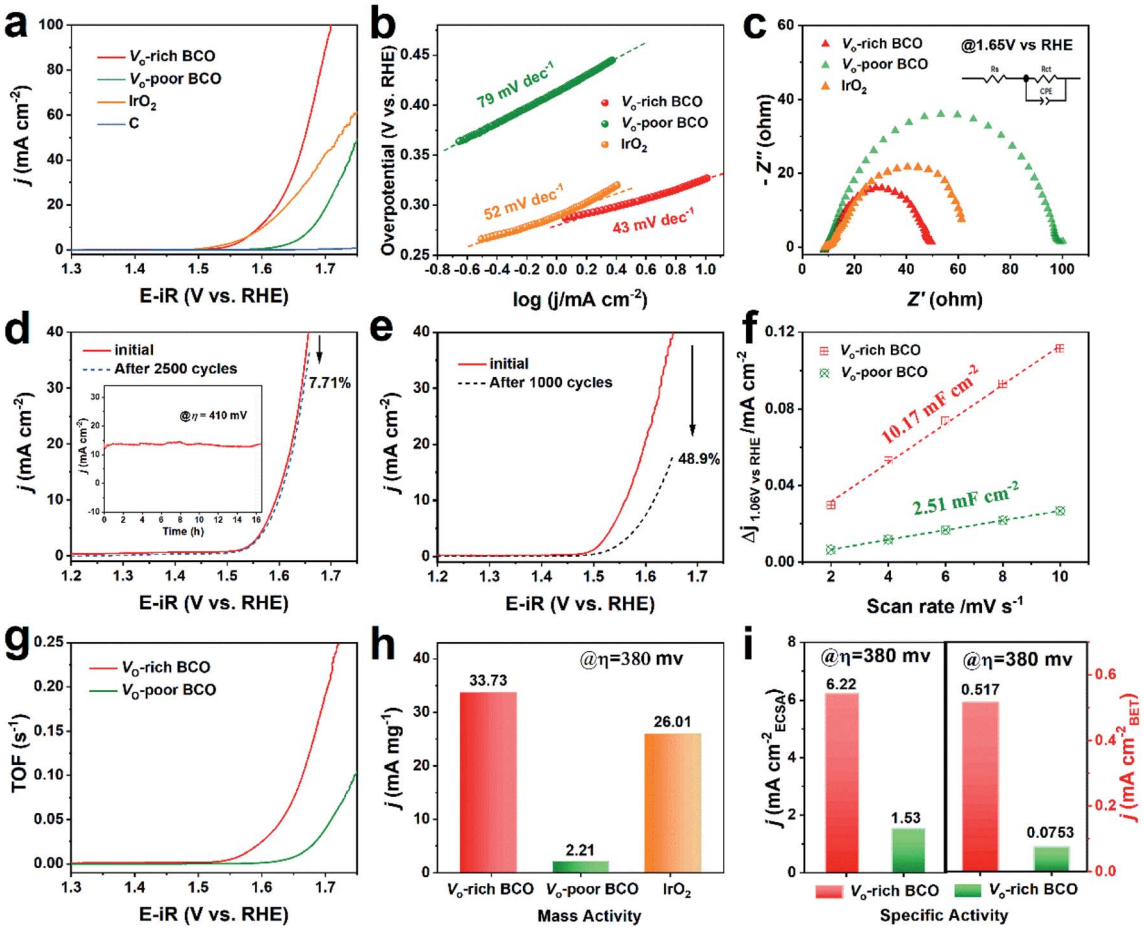

Fig. 3 (a) LSV curves of the as-prepared catalysts at a scan rate of 5 mV s^{-1}. (b) Tafel plot of the as-prepared catalysts. (c) Nyquist plots and the fitting equivalent circuit model. LSV curves of (d) the V_o-rich BCO curve and (e) IrO_2 catalysts initially and after 2500 cycles and 1000 cycles, respectively. The inset shows the chronoamperometric *i*–*t* curves of V_o-rich BCO at an overpotential of 410 mV (*vs.* RHE). (f) Current density as a function of scan rate. (g) TOF curves of the as-prepared catalysts. (h) The mass activity and (i) specific activity normalized by BET and ECSA at an overpotential $\eta = 380$ mV, respectively.

mV) and V_o-poor BCO (overpotential of 452 mV), respectively. In addition, the current density of V_o-rich BCO (89 mA cm^{-2}) at 1.7 V *versus* RHE greatly surpasses that of IrO_2 (36 mA cm^{-2}) and V_o-poor BCO (18 mA cm^{-2}), which is strongly reflected by its small Tafel slope of 43 mV dec^{-1} (in Fig. 3b). The Tafel slope of V_o-rich BCO is smaller than that of V_o-poor BCO (79 mV dec^{-1}) and benchmark IrO_2 (52 mV dec^{-1}), suggesting that it has faster reaction kinetics and better activity than those of V_o-poor BCO. Fig. 3c shows the electrochemical impedance (EIS) spectra of those catalysts to study the charge transfer process. The semicircle diameter in the high-frequency range of Nyquist plots corresponding to the charge transfer resistance (R_{ct}) shows that the resistance of V_o-rich BCO (39 Ω) is much lower than that of V_o-poor BCO (88 Ω). It highly indicates that V_o-rich BCO possesses a faster charge transfer and more facile kinetics for OER catalysts. In conclusion, higher OER activity is observed in V_o-rich BCO.

The stability of V_o-rich BCO was checked by chronoamperometry measurement at a constant potential η = 410 mV. The current density slightly fluctuates after a 12 h test and the relative retention of current density is about 98% (inset in Fig. 3d). To further verify the long-term stability, continuous potential cycling between 1.011 and 1.811 (*versus* RHE) at a scan rate of 100 mV s^{-1} was performed for the V_o-rich BCO. After 2500 cycles, the electrochemical properties are still retained well with only a 7.71% decrease, while there is a rapid degradation of current density in the benchmark IrO_2 after 1000 cycles of about 48.9% (Fig. 3e) due to the formation of highly oxidized iridium in alkaline electrolyte.[14] Further evidence of the V_o-rich BCO catalyst stability against the OER came from the HRTEM image in Fig. S9.† The HRTEM image of V_o-rich BCO before and after OER testing confirms that the surfaces of the catalysts retain a crystalline structure. The distinct behavior of V_o-rich BCO and IrO_2 catalysts strongly demonstrates the stability of V_o-rich BCO under alkaline conditions. The significant improvement in the stability of V_o-rich BCO is likely due to the interaction between metal species and oxygen species in the tetrahedral structure as well as the strong Co–O bond of V_o-rich BCO.[32] Subsequently, the O K-edge and Co L-edge XAS measurements of V_o-rich BCO before and after long-term stability tests were conducted to characterize the changes of electronic structure in the OER. As seen in Fig. S10,† the oxidation states of Co for V_o-rich BCO catalysts are almost the same. The intensity ratio of feature 'B' to feature 'A' of the catalysts after the OER process is higher than that of the initial catalysts. According to the above section analysis, peak B relates to the covalence between transition metal Co 3d and O 2p, and oxygen is redox-active. Therefore, the active oxygen is significantly increased *via* oxygen incorporation and evolution, which suggests that lattice oxygen may directly participate in the OER.

To further understand the origin of high activity of V_o-rich BCO, the double-layer capacitance (C_{dl}) which is directly related to the electrochemical surface area (ECSA) of the as-prepared catalysts was measured. The C_{dl} of 10.17 mF cm^{-2} for V_o-rich BCO is about 4 times larger than that of V_o-poor BCO, indicating that more accessible active sites are created in V_o-rich BCO *via* oxygen defect modulation (in Fig. 3f and S11†). Such higher OER activity is also demonstrated by the analysis of the turnover frequency (TOF) of O_2 molecules evolved per second per active site for the studied catalysts; as shown in Fig. 3g, a TOF of 0.0317 s^{-1} has been recorded for V_o-rich BCO catalysts, which is about 18 times that of V_o-poor BCO catalysts (0.0018 s^{-1}) at η = 380 mV. Therefore, the outstanding activity of V_o-rich BCO greatly promotes OER performance. Furthermore, Fig. 3h shows that the mass activity (current density/electrocatalyst loading) of V_o-rich BCO is about 15 times higher than that of the V_o-poor BCO catalyst, and about 1.3 times higher than that of the IrO_2 catalyst at η = 380 mV. To exclude geometric effects, the OER current density is normalized by BET as displayed in Fig. 3i. The specific activity normalized by BET of the V_o-rich BCO catalyst is about 7 times higher than that of V_o-poor BCO. Meanwhile, the specific activity normalized by the ECSA on V_o-rich BCO still greatly outperforms that on V_o-poor BCO at η = 380 mV, which is about 4 times higher for current density, clearly indicating that the OER activity is greatly enhanced in V_o-rich BCO. The excellent catalytic activity for the OER in V_o-rich BCO is superior to those of most of the state-of-the-art oxide-based catalysts ever reported (Table S6†). All the results demonstrate that the much improved OER performance of V_o-rich BCO probably originates from increased oxygen vacancies, indicating a possible reaction mechanism change. Some previous studies reveal that the switch of the OER mechanism from AEM to LOM can decrease the free energy barrier to promote the catalytic activity due to the direct O–O coupling.[9,13–15] The experimental validation of such a lattice oxygen participation mechanism is discussed in the following section.

Chemical recognition of peroxide active species (O_2^{2-})

The conventional understanding of AEM on oxides involves four concerted proton–electron transfer steps on metal-ion centers at their surface.[9,15,16] The OER proceeding on oxides *via* the participation of lattice oxygen typically exhibits pH-dependent activity, which results from the mismatch between the electron transfer kinetics and hydroxide affinity at the oxide/electrolyte interface, reflecting the non-concerted proton–electron transfer.[39,40] The V_o-poor BCO shows negligible pH dependence (Fig. S12†), while the V_o-rich BCO exhibits a strong pH dependence of catalytic activity in Fig. 4a. Moreover, the current densities of V_o-rich BCO at 1.65 V *versus* RHE as a function of pH value are much higher than those of V_o-poor BCO (Fig. 4b), indicating that the non-concerted proton–electron transfer process for the OER can be triggered at a low concentration of hydroxyl ions. These results are consistent with previous reports about Zn–Co oxyhydroxide, $SrCoO_{3-\delta}$, $La_{0.5}Sr_{0.5}CoO_{3-\delta}$, and $Pr_{0.5}Ba_{0.5}CoO_{3-\delta}$ metal oxides.[9,14,15]

Recognition of peroxo-like (O_2^{2-}) and superoxo-like (O_2^{-}) negative species can provide indirect evidence for the proposed LOM route.[41] According to a previous report,[42] O_2^{2-} is thermodynamically more stable than O_2^{-}; thus probing the negative O_2^{2-} species is viable and significant to indirectly verify the lattice oxygen participation during the OER process. To track these O_2^{2-} species from the LOM process, the tetramethylammonium cation (TMA^+) was selected as the chemical probe

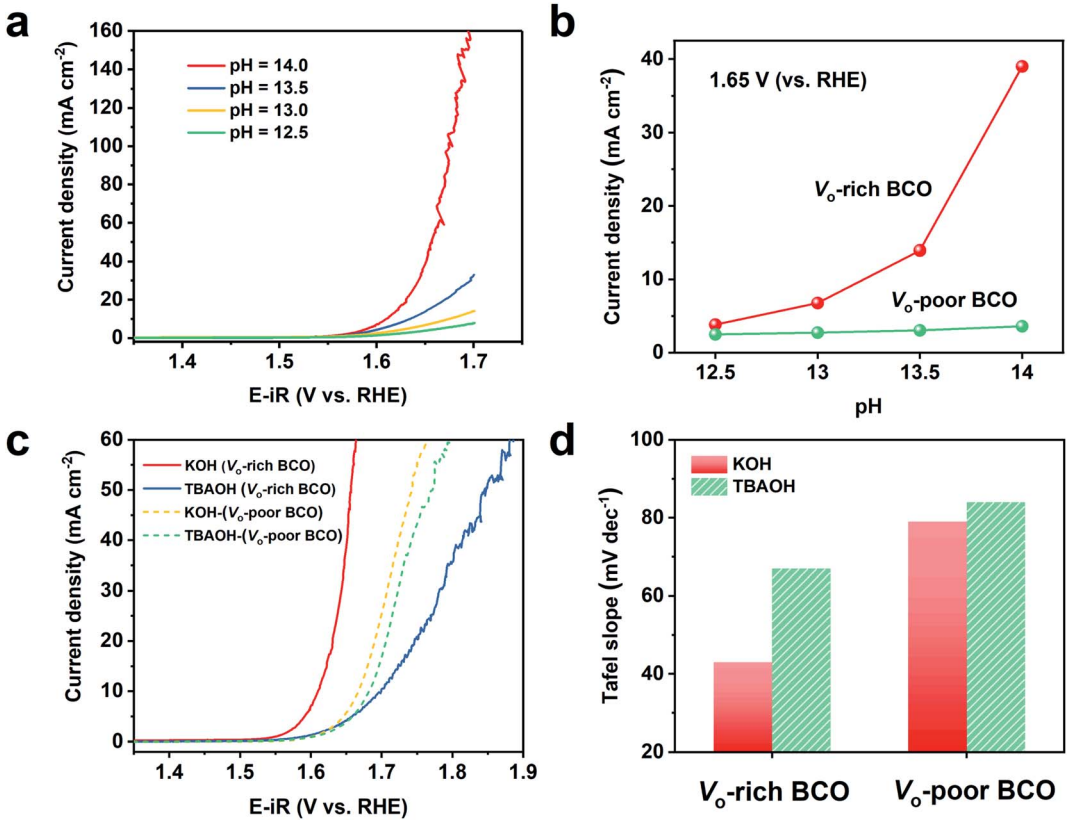

Fig. 4 (a) pH dependence of the OER activities of V_o-rich BCO. (b) Current densities of V_o-rich BCO and V_o-poor BCO at 1.65 V *versus* RHE as a function of pH value. (c) Polarization curves and (d) derived Tafel slope of V_o-rich BCO and V_o-poor BCO in 1.0 M KOH and TMAOH dissolved in H_2O, respectively.

owing to its specific interaction with negative oxygenated species. As seen in Fig. 4c, with the adding of TMAOH, the catalytic OER activity is greatly reduced in V_o-rich BCO and its Tafel slope increases from 43 to 67 mV dec^{-1}, while the variations of LSV curve and Tafel slope (from 79 to 83 mV dec^{-1}) are slight in V_o-poor BCO (Fig. 4d). This indicates that TMA^+ can strongly bind to the *in situ* generated negative O_2^{2-} species on the V_o-rich BCO surface to inhibit the LOM process during electrocatalytic water oxidation. These experimental results are consistent with previous statements that the OER proceeded on V_o-rich BCO oxide *via* the participation of lattice oxygen.

The oxygen vacancy defects that are crucial in improving OER activity and enhancing the electrocatalysis of oxygen on BCO surfaces have been identified. As for the origins of this improvement, the quite important and essential factor is lattice oxygen activation by electronic and crystal structure modulation, induced by surface oxygen vacancies, which can enhance the hybridization of Co 3d and O 2p. Based on the report of accessible lattice vacancy sites of $La_{1-x}Sr_xCoO_{3-\delta}$,[14] the high content of oxygen vacancies in V_o-rich BCO may be beneficial to increase the tendency for oxygen intercalation and cause facile oxygen ion diffusion. The diffusion rates of oxygen ions in BCO catalysts were measured chronoamperometrically based on a bound 3D solid-state diffusion model in air saturated 1.0 M KOH.[14,43–45] As presented in Fig. S13,† V_o-rich BCO has a diffusion rate of 3.13×10^{-14} cm^2 s^{-1} at room temperature, which is about 3 times faster than the diffusion rate of 1.09×10^{-14} cm^2 s^{-1} in V_o-poor BCO, which is beneficial to enhance conductivity.

Furthermore, the V_o-rich BCO has low charge transfer resistance and consequently accelerates electron transfer, which is demonstrated by the work function of V_o-rich BCO and V_o-poor BCO (Fig. 5a). The V_o-rich BCO shows a smaller work function and higher electron transfer ability. In addition, the samples were pressed into thin slices under 10 MPa and then the oxygen ion diffusion rate was measured at 400 °C (Fig. S14†); the diffusion rate in V_o-rich BCO is still faster than that in V_o-poor BCO. The fast diffusion rate represents the lower boundary on the mobility of oxygen at the surface. Therefore, increasing the mobility of oxygen in V_o-rich BCO can significantly promote conductivity. The electrical conductivity was also measured at room temperature by the four-probe method. As shown in Fig. S15,† the electrical conductivity of V_o-rich BCO is almost 3 times higher than that of V_o-poor BCO, indicating a significant conductivity improvement by increasing the oxygen vacancy. These enhanced conductivity experimental results can be observed in the PDOS of Fig. S6;† the state density around the Fermi energy level of V_o-rich BCO is apparently larger than that of V_o-poor BCO, which is favorable for the electron conductivity. Therefore, the significant improvement of conductivity in V_o-rich BCO is another factor for enhancing the OER performance.

Based on the above results, the OER catalytic activity is found to correlate with lattice oxygen activation and conductivity

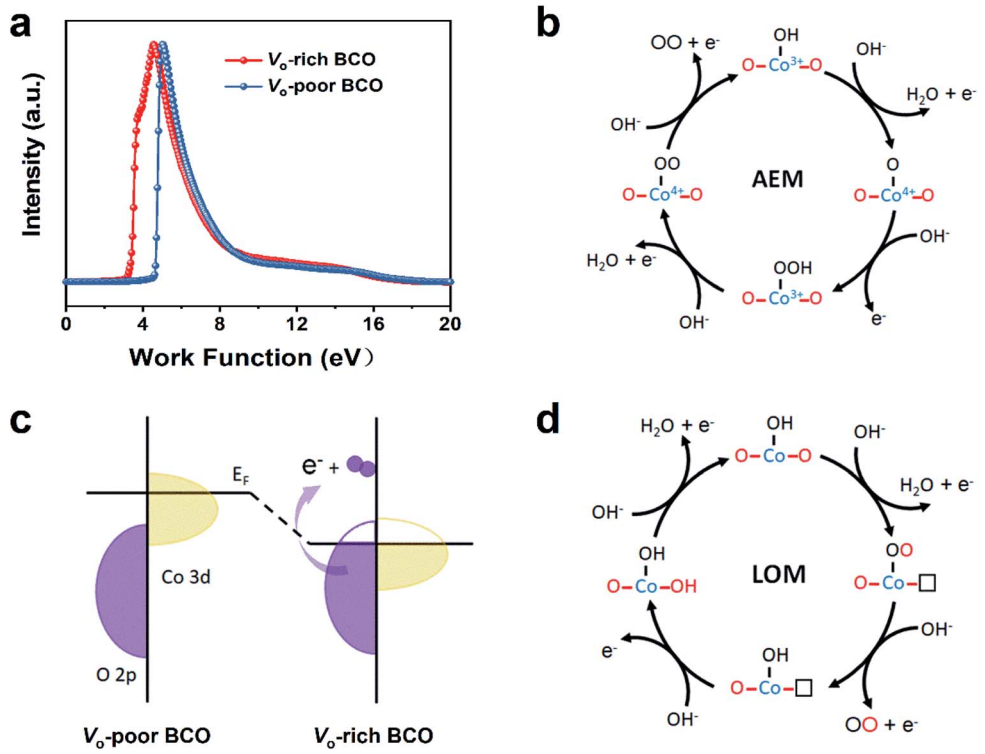

Fig. 5 (a) Ultraviolet-photoelectron spectra of V_o-rich BCO and V_o-poor BCO. Proposed OER mechanisms, including (b) AEM and (d) LOM. The empty square represents the oxygen vacancy. (c) Schematic energy band diagrams for V_o-rich BCO and V_o-poor BCO.

induced by the oxygen vacancy. Meanwhile, taking two different reaction routes and mechanisms into consideration, the LOM can decrease the free energy barrier to promote the catalytic activity due to the direct O–O coupling, compared with the AEM.[9,10,14] Thus the enhanced OER catalytic activity originates mainly from the reaction mechanism change, related to the exchange of lattice oxygen species participating in the water electrolysis. The AEM only relates to the redox activity of the surface transition metal, and the reaction route involves four concerted proton–electron transfer steps (Fig. 5b): O–Co–O + OH^- → O–Co(OH–)–O + H_2O + e^- + OH^- → O–Co(O^{2-})–O + H_2O + e^- + OH^- → O–Co(OOH$^-$)–O + H_2O + e^- + OH^- → O–Co(OO^{2-})–O → O–Co–O + O_2. With the increase of oxygen vacancies, the overlap between d-orbitals of the Co atom and p-orbitals of the O atom gradually increases. When the overlap is high enough, ligand holes can be formed and the Fermi level can be modulated through the strongly hybridized Co 3d–O 2p band[14] (schematically shown in Fig. 5c). The OER on oxygen sites can be triggered when the Fermi level becomes pinned to the top of the O 2p band for V_o-rich oxides, resulting in electronic states with substantial O 2p character near the Fermi level. As a result, the lattice oxygen can take part in a redox reaction, which is in accordance with the highly oxidative oxygen species (O_2^{2-}/O^-) results of XPS and the redox-active oxygen results of O K-edge XAS, as well as the computed results of PDOS. The facts of pH dependence of catalytic activity and chemical probing of O_2^{2-} with TMAOH indicate that non-concerted proton–electron transfer steps are coupled to the activation of lattice oxygen redox reactions, and thus the OER of V_o-rich BCO follows a LOM route with non-concerted proton–electron transfer steps (Fig. 5d). The possible deprotonation (HO–Co(O)–OH + OH^- → HO–Co(O)–O + H_2O) proceeds after the decoupled electron transfer during the release of oxygen (O–Co(O)–O → O–Co–(OO)– + OH^- → O–Co(OH^-)– + O_2 + e^-, where the empty square represents oxygen vacancy). Therefore, on the one hand, the oxygen vacancy on the surface promotes the oxygen ion diffusion and increases conductivity; on the other hand, the oxygen vacancy defects can weaken the coulombic force between neighboring lattice oxygen and metal Co ions, making the bonded oxygen atom highly activated, which results in lattice oxygen participating in the electrocatalytic water oxidation to decrease the barrier and boost the OER process.

Conclusion

In summary, oxygen-vacancy-rich $(Bi_{0.5}Co_{0.5})_2O_3$ was prepared and exhibits enhanced OER activity in terms of overpotential (367 mA cm^{-2}), Tafel slope (43 mV dec^{-1}) and excellent long-term stability in alkaline media, surpassing greatly the benchmark IrO_2. The increase of oxygen vacancy can lower the Fermi energy, increase the overlap of Co 3d and O 2p, and weaken the coulombic force between neighboring lattice oxygen and metal Co ions. As a result, the OER mechanism will switch from AEM to LOM, which is confirmed by the pH-dependent activity and chemical probe analysis. On the other hand, the oxygen vacancy can increase the oxygen ionic diffusion rate and conductivity. This work provided a new approach to engineer highly active and stable catalysts towards water oxidation involving lattice oxygen *via* surface defect and crystal structure modulation.

Author contributions

Zhengping Fu and Yalin Lu designed this project. Huan Liu conceived and performed the experiments. Xiaoning Li and Cailing Peng provided very useful advice and discussion. Huiru Cheng and Bangjiao Ye conducted the positron annihilation measurements. Liuyang Zhu, Yuanxi Zhang, Yingying Zhang, and Qingmei Wu conducted XRD, SEM, and TEM measurements. Wei Zou, Haoliang Huang, and Jianlin Wang performed XAS characterization and analyzed some data. Jiameng Cui carried out the electrical conductivity measurement. Zezhi Chen and Wen Gu performed the XRD refinement. Zhengping Fu and Huan Liu wrote the manuscript.

Conflicts of interest

The authors declare no conflicts of interest.

Acknowledgements

This work was financially supported by the National Key Research and Development Program of China (2016YFA0401004), the National Natural Science Foundation of China (51627901), Anhui Initiative in Quantum Information Technologies (AHY100000), Anhui Provincial Natural Science Foundation (1908085ME119) and the Open Programs for the Key Science & Technology Infrastructures of Chinese Academy of Sciences.

Notes and references

1 W. Wang, Y. Yang, D. Huan, L. Wang, N. Shi, Y. Xie, C. Xia, R. Peng and Y. Lu, An Excellent OER Electrocatalyst of Cubic $SrCoO_3$ Prepared by A Simple F-Doping Strategy, *J. Mater. Chem. A*, 2019, **7**, 12538–12546.

2 X. Li, Y. Sun, Q. Wu, H. Liu, W. Gu, X. Wang, Z. Cheng, Z. Fu and Y. Lu, Optimized Electronic Configuration to Improve the Surface Absorption and Bulk Conductivity for Enhanced Oxygen Evolution Reaction, *J. Am. Chem. Soc.*, 2019, **141**, 3121–3128.

3 S. Niu, W.-J. Jiang, Z. Wei, T. Tang, J. Ma, J.-S. Hu and L.-J. Wan, Se-Doping Activates FeOOH for Cost-Effective and Efficient Electrochemical Water Oxidation, *J. Am. Chem. Soc.*, 2019, **141**, 7005–7013.

4 J. Hwang, R. R. Rao, L. Giordano, Y. Katayama, Y. Yu and Y. Shao-Horn, Perovskites in Catalysis and Electrocatalysis, *Science*, 2017, **358**, 751–756.

5 M. Busch, Water Oxidation: From Mechanisms to Limitations, *Curr. Opin. Electrochem.*, 2018, **9**, 278–284.

6 F. Song, L. Bai, A. Moysiadou, S. Lee, C. Hu, L. Liardet and X. Hu, Transition Metal Oxides as Electrocatalysts for the Oxygen Evolution Reaction in Alkaline Solutions: An Application-Inspired Renaissance, *J. Am. Chem. Soc.*, 2018, **140**, 7748–7759.

7 N. Govindarajan, J. M. García-Lastra, E. J. Meijer and F. Calle-Vallejo, Does the Breaking of Adsorption-Energy Scaling Relations Guarantee Enhanced Electrocatalysis, *Curr. Opin. Electrochem.*, 2018, **8**, 110–117.

8 N. B. Halck, V. Petrykin, P. Krtil and J. Rossmeisl, Beyond the Volcano Limitations in Electrocatalysis – Oxygen Evolution Reaction, *Phys. Chem. Chem. Phys.*, 2014, **16**, 13682–13688.

9 Z.-F. Huang, J. Song, Y. Du, S. Xi, S. Dou, J. M. V. Nsanzimana, C. Wang, Z. J. Xu and X. Wang, Chemical and Structural Origin of Lattice Oxygen Oxidation in Co–Zn Oxyhydroxide Oxygen Evolution Electrocatalysts, *Nat. Energy*, 2019, **4**, 329–338.

10 S. Yagi, I. Yamada, H. Tsukasaki, A. Seno, M. Murakami, H. Fujii, H. Chen, N. Umezawa, H. Abe, N. Nishiyama and S. Mori, Covalency-reinforced oxygen evolution reaction catalyst, *Nat. Commun.*, 2015, **6**, 8249.

11 X. Rong, J. Parolin and A. M. Kolpak, A Fundamental Relationship between Reaction Mechanism and Stability in Metal Oxide Catalysts for Oxygen Evolution, *ACS Catal.*, 2016, **6**, 1153–1158.

12 J. S. Yoo, X. Rong, Y. Liu and A. M. Kolpak, Role of Lattice Oxygen Participation in Understanding Trends in the Oxygen Evolution Reaction on Perovskites, *ACS Catal.*, 2018, **8**, 4628–4636.

13 J. S. Yoo, Y. Liu, X. Rong and A. M. Kolpak, Electronic Origin and Kinetic Feasibility of the Lattice Oxygen Participation During the Oxygen Evolution Reaction on Perovskites, *J. Phys. Chem. Lett.*, 2018, **9**, 1473–1479.

14 J. T. Mefford, X. Rong, A. M. Abakumov, W. G. Hardin, S. Dai, A. M. Kolpak, K. P. Johnston and K. J. Stevenson, Water Electrolysis on $La_{1-x}Sr_xCoO_{3-\delta}$ Perovskite Electrocatalysts, *Nat. Commun.*, 2016, **7**, 11053.

15 A. Grimaud, O. Diaz-Morales, B. Han, W. T. Hong, Y.-L. Lee, L. Giordano, K. A. Stoerzinger, M. T. M. Koper and Y. Shao-Horn, Activating Lattice Oxygen Redox Reactions in Metal Oxides to Catalyse Oxygen Evolution, *Nat. Chem.*, 2017, **9**, 457–465.

16 X. Li, H. Wang, Z. Cui, Y. Li, S. Xin, J. Zhou, Y. Long, C. Jin and J. B. Goodenough, Exceptional Oxygen Evolution Reactivities on $CaCoO_3$ and $SrCoO_3$, *Sci. Adv.*, 2019, **5**, eaav6262.

17 J. Liu, E. Jia, L. Wang, K. A. Stoerzinger, H. Zhou, C. S. Tang, X. Yin, X. He, E. Bousquet, M. E. Bowden, A. T. S. Wee, S. A. Chambers and Y. Du, Tuning the Electronic Structure of $LaNiO_3$ through Alloying with Strontium to Enhance Oxygen Evolution Activity, *Adv. Sci.*, 2019, **6**, 1901073.

18 C. Hu, X. Wang, T. Yao, T. Gao, J. Han, X. Zhang, Y. Zhang, P. Xu and B. Song, Enhanced Electrocatalytic Oxygen Evolution Activity by Tuning Both the Oxygen Vacancy and Orbital Occupancy of B-Site Metal Cation in $NdNiO_3$, *Adv. Funct. Mater.*, 2019, **29**, 1902449.

19 Z. Cai, Y. Bi, E. Hu, W. Liu, N. Dwarica, Y. Tian, X. Li, Y. Kuang, Y. Li, X.-Q. Yang, H. Wang and X. Sun, Single-Crystalline Ultrathin Co_3O_4 Nanosheets with Massive Vacancy Defects for Enhanced Electrocatalysis, *Adv. Energy Mater.*, 2018, **8**, 1701694.

20 L. Zhuang, L. Ge, Y. Yang, M. Li, Y. Jia, X. Yao and Z. Zhu, Ultrathin Iron-Cobalt Oxide Nanosheets with Abundant

Oxygen Vacancies for the Oxygen Evolution Reaction, *Adv. Mater.*, 2017, **29**, 1606793.

21 R. Wu, B. Xiao, Q. Gao, Y. Zheng, X. Zheng, J. Zhu, M. Gao and S. Yu, A Janus Nickel Cobalt Phosphide Catalyst for High-Efficiency Neutral-pH Water Splitting, *Angew. Chem.*, 2018, **130**, 15671–15675.

22 H. Guo, Q. Feng, K. Xu, J. Xu, J. Zhu, C. Zhang and T. Liu, Self-Templated Conversion of Metallogel into Heterostructured TMP@Carbon Quasiaerogels Boosting Bifunctional Electrocatalysis, *Adv. Funct. Mater.*, 2019, **29**, 1903660.

23 M. Risch, A. Grimaud, K. J. May, K. A. Stoerzinger, T. J. Chen, A. N. Mansour and Y. Shao-Horn, Structural Changes of Cobalt-Based Perovskites upon Water Oxidation Investigated by EXAFS, *J. Phys. Chem. C*, 2013, **117**, 8628–8635.

24 K. J. May, C. E. Carlton, K. A. Stoerzinger, M. Risch, J. Suntivich, Y.-L. Lee, A. Grimaud and Y. Shao-Horn, Influence of Oxygen Evolution during Water Oxidation on the Surface of Perovskite Oxide Catalysts, *J. Phys. Chem. Lett.*, 2012, **3**, 3264–3270.

25 A. Grimaud, K. J. May, C. E. Carlton, Y.-L. Lee, M. Risch, W. T. Hong, J. Zhou and Y. Shao-Horn, Double Perovskites as A Family of Highly Active Catalysts for Oxygen Evolution in Alkaline Solution, *Nat. Commun.*, 2013, **4**, 2439.

26 Y. Zhu, H. A. Tahini, Z. Hu, Z. Chen, W. Zhou, A. C. Komarek, Q. Lin, H. Lin, C. Chen, Y. Zhong, M. T. Fernández-Díaz, S. C. Smith, H. Wang, M. Liu and Z. Shao, Boosting Oxygen Evolution Reaction by Creating Both Metal Ion and Lattice-Oxygen Active Sites in a Complex Oxide, *Adv. Mater.*, 2020, **32**, 1905025.

27 A. Grimaud, W. T. Hong, Y. Shao-Horn and J.-M. Tarascon, Anionic Redox Processes for Electrochemical Devices, *Nat. Mater.*, 2016, **15**, 121–126.

28 M. Li, M. J. Pietrowski, R. A. De Souza, H. Zhang, I. M. Reaney, S. N. Cook, J. A. Kilner and D. C. Sinclair, A Family of Oxide Ion Conductors Based on the Ferroelectric Perovskite $Na_{0.5}Bi_{0.5}TiO_3$, *Nat. Mater.*, 2014, **13**, 31–35.

29 S. Liu, X. F. Lu, J. Xiao, X. Wang and X. W. Lou, Bi_2O_3 Nanosheets Grown on Multi-Channel Carbon Matrix to Catalyze Efficient CO_2 Electroreduction to HCOOH, *Angew. Chem., Int. Ed.*, 2019, **58**, 13828–13833.

30 X. Li, H. Liu, Z. Chen, Q. Wu, Z. Yu, M. Yang, X. Wang, Z. Cheng, Z. Fu and Y. Lu, Enhancing Oxygen Evolution Efficiency of Multiferroic Oxides by Spintronic and Ferroelectric Polarization Regulation, *Nat. Commun.*, 2019, **10**, 1409.

31 Z. Chen, T. Hong, Z. Wang, J. Wang, H. Huang, R. Peng, W. Yan, Z. Fu, K. S. Brinkman and Y. Lu, Anisotropic Magnetic Property and Exchange Bias Effect in A Homogeneous Sillen–Aurivillius Layered Oxide, *J. Eur. Ceram. Soc.*, 2019, **39**, 2685–2691.

32 Y. Zhu, W. Zhou, J. Sunarso, Y. Zhong and Z. Shao, Engineering Highly Sctive Oxygen Sites in Perovskite Oxides for Stable and Efficient Oxygen Evolution, *Adv. Funct. Mater.*, 2016, **26**, 5862–5872.

33 J. Xiong, H. Zhong, J. Li, X. Zhang, J. Shi, W. Cai, K. Qu, C. Zhu, Z. Yang, S. P. Beckman and H. Cheng, Phosphorus-Doped Perovskite Oxide as Highly Efficient Water Oxidation Electrocatalyst in Alkaline Solution, *Appl. Catal. B Environ.*, 2019, **256**, 117817.

34 C. Chen, J. Avila, E. Frantzeskakis, A. Levy and M. C. Asensio, Observation of A Two-Dimensional Liquid of Fröhlich Polarons at the Bare $SrTiO_3$ Surface, *Nat. Commun.*, 2015, **6**, 8585.

35 M. Kong, Y. Li, X. Chen, T. Tian, P. Fang, F. Zheng and X. Zhao, Tuning the Relative Concentration Ratio of Bulk Defects to Surface Defects in TiO_2 Nanocrystals Leads to High Photocatalytic Efficiency, *J. Am. Chem. Soc.*, 2011, **133**, 16414–16417.

36 Z.-Y. Yu, Y. Duan, J.-D. Liu, Y. Chen, X.-K. Liu, W. Liu, T. Ma, Y. Li, X.-S. Zheng, T. Yao, M.-R. Gao, J.-F. Zhu, B.-J. Ye and S.-H. Yu, Unconventional CN Vacancies Suppress Iron-Leaching in Prussian Blue Analogue Pre-Catalyst for Boosted Oxygen Evolution Catalysis, *Nat. Commun.*, 2019, **10**, 2799.

37 Y. Liu, H. Cheng, M. Lyu, S. Fan, Q. Liu, W. Zhang, Y. Zhi, C. Wang, C. Xiao, S. Wei, B. Ye and Y. Xie, Low Overpotential in Vacancy-Rich Ultrathin $CoSe_2$ Nanosheets for Water Oxidation, *J. Am. Chem. Soc.*, 2014, **136**, 15670–15675.

38 X. Liu, K. Zhou, L. Wang, B. Wang and Y. Li, Oxygen Vacancy Clusters Promoting Reducibility and Activity of Ceria Nanorods, *J. Am. Chem. Soc.*, 2009, **131**, 3140–3141.

39 L. Giordano, B. Han, M. Risch, W. T. Hong, R. R. Rao, K. A. Stoerzinger and Y. Shao-Horn, pH Dependence of OER Activity of Oxides: Current and Future Perspectives, *Catal. Today*, 2016, **262**, 2–10.

40 T. Liu, M. Guo, A. Orthaber, R. Lomoth, M. Lundberg, S. Ott and L. Hammarström, Accelerating Proton-Coupled Electron Transfer of Metal Hydrides in Catalyst Model Reactions, *Nat. Chem.*, 2018, **10**, 881–887.

41 G. Assat and J.-M. Tarascon, Fundamental Understanding and Practical Challenges of Anionic Redox Activity in Li-Ion Batteries, *Nat. Energy*, 2018, **3**, 373–386.

42 C. Yang, O. Fontaine, J.-M. Tarascon and A. Grimaud, Chemical Recognition of Active Oxygen Species on the Surface of Oxygen Evolution Reaction Electrocatalysts, *Angew. Chem.*, 2017, **129**, 8778–8782.

43 F. R. Van Buren, G. H. J. Broers, A. J. Bouman and C. Boesveld, An Electrochemical Method for the Determination of Oxygen Ion Diffusion Coefficients in $La_{1-x}Sr_xCoO_{3-y}$ Compounds, *J. Electroanal. Chem. Interfacial Electrochem.*, 1978, **87**, 389–394.

44 A. G. C. Kobussen, F. R. van Buren and G. H. J. Broers, The Influence of the Particle Size Distribution on the Measurement of Oxygen Ion Diffusion Coefficients in $La_{0.50}Sr_{0.50}CoO_{3-y}$, *J. Electroanal. Chem. Interfacial Electrochem.*, 1978, **91**, 211–217.

45 A. Nemudry, E. L. Goldberg, M. Aguirre and M. Á. Alario-Franco, Electrochemical Topotactic Oxidation of Nonstoichiometric Perovskites at Ambient Temperature, *Solid State Sci.*, 2002, **4**, 677–690.